Bayesian inference on the Allee effect in cancer cell populations using time-lapse microscopy images

Journal of Theoretical Biology 574 (2023) 111624

Contents lists available at ScienceDirect

Journal of Theoretical Biology

journal homepage: www.elsevier.com/locate/yjtbi

Bayesian inference on the Allee effect in cancer cell line populations using time-lapse microscopy images

Gustav Lindwall *, Philip Gerlee

Chalmers tvärgata 3, 412 58 Gothenburg, Sweden

ARTICLE INFO

Keywords:
Agent based models/individual based model
MCMC
Population size
Reaction–diffusion mechanisms
Stochastic differential equations
Cancer modelling

ABSTRACT

The Allee effect describes the phenomenon that the per capita reproduction rate increases along with the population density at low densities. Allee effects have been observed at all scales, including in microscopic environments where individual cells are taken into account. This is great interest to cancer research, as understanding critical tumour density thresholds can inform treatment plans for patients. In this paper, we introduce a simple model for cell division in the case where the cancer cell population is modelled as an interacting particle system. The rate of the cell division is dependent on the local cell density, introducing an Allee effect. We perform parameter inference of the key model parameters through Markov Chain Monte Carlo, and apply our procedure to two image sequences from a cervical cancer cell line. The inference method is verified on *in silico* data to accurately identify the key parameters, and results on the *in vitro* data strongly suggest an Allee effect

1. Introduction

The Allee effect is a phenomena in ecology, noting that a population's growth rate often is a function of its density. More precisely, the per capita growth rate increases along with the population density until a maximum is reached at an optimal population density. After passing this density, the per capita reproduction rate diminishes, eventually becoming zero at the carrying capacity. The underlying mechanics giving rise to an Allee effect are for example difficulty finding mates, lack of protection from predators and lessened production of public goods facilitating population growth (Courchamp et al., 2008). In bio-conservation applications, determining the threshold for when a population becomes unsustainable and risks extinction is of dire importance to mitigate biodiversity collapse as a result of human action, e.g deforestation and over-fishing.

In recent years, microbiological systems have increasingly been understood and modelled in terms of ecosystems of normal cells (Basanta and Anderson, 2013). In this context, cancer growth functions akin to an invasive species. This has spurred a flurry of research into both how one can understand cancer in terms of theory from mathematical ecology, and how one can use this knowledge to devise novel cancer therapies.

1.1. Mathematical models of population growth

We will now give a brief history of population dynamics modelling, building up to a few proposals for Allee effect expressions found in the literature. Let $N(t)$ be the size of some population at time t. A deterministic mean-field model of population growth takes the form

$$\frac{\mathrm{d}N(t)}{\mathrm{d}t} = N(t)R(N(t)). \tag{1.1}$$

where $R(\cdot)$ models the per-capita reproduction rate as a function of the population size. No spatial structure of the population is taken into account, it is assumed to be 'well-mixed' in whatever homogeneous environment it resides in. Ordinary differential equations such as (1.1) can exhibit *steady states*, found by solving $NR(N) = 0$. Depending on the initial condition, $N(t)$ will approach one of the steady states as $t \to \infty$. For example, we can consider $R(N) = r(1 - N/K) - d$, which gives logistic growth with constant death rate;

$$\frac{\mathrm{d}N(t)}{\mathrm{d}t} = rN(t)\left(1 - \frac{N(t)}{K}\right) - dN(t). \tag{1.2}$$

Here r is a baseline reproduction rate, K is the carrying capacity and $d < r$ is the death rate. This equation exhibits two steady states; $N_1 = 0$ and $N_2 = K(r-h)/r$. N_1 is an unstable fix-point of the dynamical system (1.2), and as such a population modelled by this equation will gravitate towards the stable fix point N_2 as $t \to \infty$. However, this model fails to take the Allee effect into account, and thus needs modification if one wishes to model the Allee effect. In ecology, a population that is below its *extinction threshold* is said to be in *extinction debt*, meaning that below the threshold extinction of the species is inevitable without

* Corresponding author.
E-mail addresses: guslindw@chalmers.se (G. Lindwall), gerlee@chalmers.se (P. Gerlee).

https://doi.org/10.1016/j.jtbi.2023.111624
Received 30 May 2023; Received in revised form 8 September 2023; Accepted 13 September 2023
Available online 27 September 2023

intervention to push it above the threshold (Tilman et al., 1994). Thus, we wish to modify $R(\cdot)$ so that an extinction threshold is accounted for in the model.

Several different strategies to mitigate this has been proposed. A natural modification would be setting (Sun, 2016)

$$R(N) = r(N - \alpha_1)(\alpha_2 - N) \tag{1.3}$$

for $\alpha_2 > |\alpha_1|$ and $\alpha_2 > 0$. $NR(N)$ now has three roots, and importantly the parabolic shape of $R(N)$ ensures a local maxima in the per capita reproduction for some N. We can divide (1.3) into two distinct cases, a *weak* and a *strong* Allee effect, depending on the roots α_1 and α_2. In the case of $\alpha_1 < 0$, the ODE

$$\frac{\mathrm{d}N(t)}{\mathrm{d}t} = rN(t)(N(t) - \alpha_1)(\alpha_2 - N(t)) \tag{1.4}$$

has a stable fix point for $N = \alpha_2$, and an unstable fix point for $N = 0$. The third root of the right-hand side of (1.4), $N = \alpha_1$, is not biologically feasible, as it corresponds to a negative population size. We call this a *weak* Allee effect, as no extinction threshold exists.

If $\alpha_1 > 0$, we obtain stable fix points for $N_1 = 0$ and $N_2 = \alpha_2$, and an unstable fix point for $N_1 = \alpha_1$, resulting in a *strong* Allee effect. The parameters α_1 and α_2 are referred to as the *lower* and *upper* Allee thresholds, and correspond to extinction and carrying capacity respectively. Extinction will eventually occur if the population size fall below α_1. If one were to include an additional death rate in (1.3), the Allee thresholds would shift, making it possible to turn a weak Allee effect into a strong one. Thus, one can for example model over-fishing using this $R(N)$, with $R(N) - d$ corresponding to harvesting at a rate d. Other models have also been proposed, for example Johnson et al. (2019), González-Olivares et al. (2006)

$$R(N) = \left(1 - \frac{N}{K}\right)\left(1 - \frac{A + \tau}{N + \tau}\right) \tag{1.5}$$

where $A < K$ here plays the part of the extinction threshold, and $\tau > 0$ is required to model a *weak* Allee effect. The derivation of (1.5) can be found in Boukal and Berec (2002), with arguments based in mate finding probability in well-mixed populations. Both of these models have been used for cancer modelling (Johnson et al., 2019; Gerlee et al., 2022; Delitala and Ferraro, 2020). In the context where we use the Allee effect as part of a cancer tumour model, harvesting in an ecological setting is akin to targeting the tumour with some drug or treatment. Thus, identifying the existence of a potential extinction threshold for a tumour can be vital when calculating dosage (Da Silva et al., 2020).

In this paper, we are more concerned with *spatial* population dynamics, where the population is not assumed to be well-mixed. Thus, instead of talking about absolute population size $N(t)$, we are concerned with individual based models where each cell constitutes an agent in an interacting particle system. There exists a rich literature on these approaches as well; in Gerlee et al. (2022) a cellular automata is used as the basis of the system. In Fadai and Simpson (2020), Fadai et al. (2020), a hexagonal lattice model is utilized, and the Allee effect is modelled using a binary switches depending on occupied neighbouring sites. Other articles studying spatial models utilizing an Allee effect include (Cassini, 2011), which focuses on its consequences in patchy population patterns.

Empirical evidence of Allee effects in cancer cell populations have been known for some time (Johnson et al., 2019), and the current understanding is that cell production of a *growth factor* upregulating the mitosis intensity of nearby cells plays an important role (Menon and Korolev, 2015); this process is called *autocrine signalling*. In Gerlee et al. (2022), the authors formulate a spatial–temporal cellular automata model taking growth factor production into account, producing an Allee effect. Our goal with this paper is to extend on the earlier work, using an agent-based model of cell migration and consider neighbour-wise interactions to explain the Allee effect.

1.2. Parameter inference on Allee effect

While we have noted a multitude of authors studying the dynamics of population models, work on fitting models to data is a less explored field. In dos Santos et al. (2015), an approach for modelling the Allee effect in agent based systems is explained, sharing many similarities to the approach taken in this article. The model fitting, however, was based on least-squares regression, with birth rate as the dependent variable and local population density as the independent variable. An inference-wise more detailed undertaking can be found in Simpson et al. (2022), where parameter identification in several proposed per-capita growth rate functions is discussed. The method used was profile-likelihood, similar to the approach taken here. However, the models discussed there were all of sigmoid-growth type, not taking a potential Allee effect into account. Finally, we can note (Morris, 2002), where measurements of proliferation rates of small mammals in different habitats was compared. The underlying model proposed was piece-wise linear, and as such linear regression was used to fit the pieces.

To our knowledge, no attempt has yet been made to take full advantage of the data available in microscopy imaging to fit an Allee effect model to cell-tracking data. We find the prospect of taking full advantage of images attractive, as it provides richer information than simply observations of density and birth rate does. In the case of imaging data being used in earlier work, the preferred method is still to use the total population number as the explanatory variable (Gerlee et al., 2022), or dividing the spatially structured data into patches (Morris, 2002). To remedy this, we have utilized an agent-based model, where the birth rate of each agent is modelled and taken into account. By using every individual detected in the imaging sequences, we hypothesize that accurate determination of the presence of an Allee effect can be determined using modest amounts of data.

The purpose of this paper is twofold. First, we construct a model for the growth of a population of cancer cells growing *in vitro*, taking into account an up-regulating effect that the tumour has on its own growth rate and how this gives rise to an Allee effect. We then justify a number of simplifications, simplifying the model as to only depend on three key parameters. In addition, a Markov Chain Monte Carlo (MCMC) algorithm is constructed to sample from the Bayesian posterior of these parameters. The algorithm is tested on *in silico* data, before applying it to a small yet high quality *in vitro* data set described in Section 5. Note that the application of our method to the *in vitro* data is in the interest of evaluating the validity of the model, rather than to draw novel conclusions from the data.

2. Model

In this section, we give an overview of our model for a public goods-derived Allee effect, and show how our per-capita reproduction rate can be derived from fairly simple calculations. We will also give an introduction to the stochastic model used for our *in silico* experiment.

2.1. Cell migration dynamics

The data set considered in this study consist of microscopy images of cancer cells. We will now discuss the inclusions and omissions made in our model, given the context of our experimental data presented in Section 5. The micro-environment surrounding the cells is fairly homogeneous, and hence we assume a complete absence of ECM or chemotaxis. Given the high resolution data of the spatial evolution of the cells, an off-lattice agent based model is a natural choice. We chose to model cell migration using stochastic differential equations (SDE:s) with isotropic diffusion in $\mathbf{R}^2$. The location $\mathbf{x}_i(t)$ of each individual cell i for $i = 1, \dots, N$ at time $t \geq 0$ evolves according to an equation

$$\mathrm{d}\mathbf{x}_i(t) = -\sum_{j \neq i} \nabla_{\mathbf{x}_i} u(\|\mathbf{x}_i(t) - \mathbf{x}_j(t)\|)\mathrm{d}t + \sigma \mathrm{d}W_i(t). \tag{2.1}$$

Table 2.1
Most of the notation used in this paper.

Variable	Explanation
$\mathbf{x}(t)$	The locations of all cancer cells at time t
i, j	Used as indices for individual cells
$\mathbf{x}_i(t)$	The location of cell i at time t
N_t	The total number of cells at time t
K	The total number of images
k	Used to talk about individual images
$\mathbf{x}_k$	The k:th image
$\mathbf{x}_{ik}$	The location of cell i in image k
β_{ik}	The number of cells born from cell i between image k and $k+1$
d_k	The number of cells who have died between image k and $k+1$
$\mathbf{X}$	Capital $\mathbf{X}$ is reserved for real data

Here $-\sum_{j\neq i}\nabla_{\mathbf{x}_i}u(\|\mathbf{x}_i(t)-\mathbf{x}_j(t)\|)$ is a drift term describing pairwise cell interactions, D is a diffusion coefficient and $W_i(t)$ is a 2-dimensional Wiener process (Klebaner, 2012). Now, let us define the number density $n(\mathbf{x},t)$ as a distribution so that for some subset $A\subset\mathbf{R}^2$,

$$\int_A n(\mathbf{x},t)\mathrm{d}\mathbf{x} = \#\text{ of cells within } A. \tag{2.2}$$

Given the large number of variables in the model we supply the reader with the below table (Table 2.1) which lists all variables and their meanings. Furthermore, we make the assumption that cells are circular, and their diameter is equal to one length unit. Both of these assumptions stem out of mathematical convenience, and are encoded in the pairwise interaction potential u.

2.2. Production of growth factor

It has been observed that some cancer cells, e.g glioblastoma, produces *growth factors* (GF) that upregulates the rate of cell division (Gerlee et al., 2022). Thus, it serves as a public good facilitating mitosis. This growth factor is produced by the cells in the culture, and undergoes a diffusion- and decay process. We describe this process in terms of a reaction–diffusion equation (Menon and Korolev, 2015)

$$\partial_t g(\mathbf{x},t) = D_g\nabla^2 g(\mathbf{x},t) + p_g n(\mathbf{x},t) - d_g g(\mathbf{x},t) \tag{2.3}$$

where $g(\mathbf{x},t)$ is the GF concentration, D_g the rate at which it diffuses, p_g its production rate and d_g its decay rate. Note that (2.3) is defined in a weak sense, since $n(\mathbf{x},t)$ is a distribution rather than a function (Hörmander, 2009). Furthermore, the length scale of (2.3) is such that cells occupy space and are counted as individuals, whereas the GF density is seen as a continuum.

Compared to the time scales at which the cell culture undergo migration and mitosis, the dynamics of growth factor occurs on a much faster time scale (Menon and Korolev, 2015). We can thus make the approximation that (2.3) is in its steady state when compared to the cell population evolution, i.e (2.3) can be written as

$$0 = D_g\nabla^2 g(\mathbf{x},t) + p_g n(\mathbf{x},t) - d_g g(\mathbf{x},t) \tag{2.4}$$

This equation can be solved by finding the fundamental solution to

$$\frac{1}{p_g}\Big(D_g\nabla^2 g(\mathbf{x},t) - d_g g(\mathbf{x},t)\Big) = 0 \tag{2.5}$$

and viewing $n(\mathbf{x},t)$ as a source term. A standard procedure gives us that

$$g(\mathbf{x},t) = \frac{p_g}{2\sqrt{D_g d_g}}\int_{\mathbf{R}^2} e^{-\sqrt{d_g/D_g}\|\mathbf{x}-\mathbf{x}'\|}n(\mathbf{x}',t)\mathrm{d}\mathbf{x}' \tag{2.6}$$

Thus, the amount of GF at $\mathbf{x}\in\mathbf{R}^2$ at some time t is given by a convolution of the number density $n(\mathbf{x},t)$ and a *kernel* $w(\mathbf{x})$ corresponding to the fundamental solution of (2.5);

$$w(\mathbf{x}) := \frac{p_g}{2\sqrt{D_g d_g}}e^{-\sqrt{d_g/D_g}\|\mathbf{x}\|}.$$

To simplify the notation, we reparameterize $w(\mathbf{x})$ using $\varepsilon = \sqrt{d_g/D_g}$ and $p_g/2d_g = C$, giving us a kernel

$$w(\mathbf{x}) = C\varepsilon e^{-\varepsilon\|\mathbf{x}\|}. \tag{2.7}$$

We will refer to ε as the *growth factor dispersion length scale* and C as the *production factor*. Let us now consider how to calculate the amount of GF around a particular cell. If all cell locations $\mathbf{x}_i$ are known at time t, we have that the density $n(\mathbf{x},t)$ is given by the empirical measure

$$n(\mathbf{x}',t)\mathrm{d}\mathbf{x}' = \mathrm{d}\mu_t(\mathbf{x}') := \sum_{i=1}^{N_t}\delta_{\mathbf{x}_i(t)}(\mathbf{x}')\mathrm{d}\mathbf{x}'$$

generated by the observation. Here $\mathbf{x}_i(t)$ is the centre of cell i, which is assumed to be a circle with diameter $r_0 = 1$. Thus, the GF-concentration stimulating a particular cell i at time t will be given by

$$g(\mathbf{x}_i(t)) = \int_{\mathbf{R}^2} w(\|\mathbf{x}_i(t)-\mathbf{x}'\|)\mathrm{d}\mu_t(\mathbf{x}') = \sum_{j=1}^{N_t} w(\|\mathbf{x}_i(t)-\mathbf{x}_j(t)\|). \tag{2.8}$$

2.3. Cell division modelling

The exact way that growth factors contribute to increased rates of cell division is complex, and depends on what stage in the cell cycle the cell in question is currently in. The simplest way to think of the GF influence on an individual cell is that it expedites the early growth of the cell, leading to DNA replication and subsequent mitosis taking place earlier (Obeyesekere et al., 1999). For the sake of our study, we will not divide the cell cycle into several different stages. Rather we will model the time from birth to division as a random variable from the exponential family, defined by a dynamic rate depending on the GF concentration. In the discussion we examine this simplification and explore more realistic approaches.

In order to model cell division, we will take inspiration from the field of reliability theory. The central object in this field is the *survival equation*. The survival equation is an ODE depending on a *rate function* $h(t)$, who's solution is the probability that some event has occurred at a time t after initiation at time t_0. Such equations are frequently used to model a large number of life length phenomena, ranging from component failures in electrical engineering to patient survival times in medical studies (Cleves et al., 2008). Here, we will use the same framework to model mitosis times. We assign a survival equation to each cell i and make its rate $h_i(t)$ a function of the local GF-concentration $g(\mathbf{x}_i(t),t)$, letting $B_i(t)$ be the probability that cell i has divided at time t after its birth at time t_0. The survival equation is given by

$$h_i(t) = \frac{B_i'(t)}{1-B_i(t)}, \quad B_i(t_0) = 0 \tag{2.9}$$

and the solution of (2.9) at time $t > t_0$ is given by

$$B_i(t) = 1-(1-B_i(t_0))\exp\Big(-\int_{t_0}^t h_i(s)\mathrm{d}s\Big) \tag{2.10}$$

$$= 1-\exp\Big(-\int_{t_0}^t h_i(s)\mathrm{d}s\Big). \tag{2.11}$$

Importantly, we see that $\int_{t_0}^t h(s)\mathrm{d}s$ gives us an accumulation of birth rate over the time interval $[t_0,t)$. We now assume that $h_i(t)$ can be factorized as $h_i(t) = J_i(t)G_i(t)$. Here $J_i(t)$ model contact inhibition, giving negative feedback to the birth rate as the local cell density increases, and $G_i(t)$ depends on the GF-concentration, providing a positive feedback. We let $G_i(t)$ be proportional to the GF present around cell i,

$$G_i(t) = \lambda g(\mathbf{x}_i(t)) \tag{2.12}$$

for some rate $\lambda > 0$. We implement contact inhibition $J_i(t)$ for cell i using an *inhibition function* $\rho_i(t)$, representing the local cell density. We calculate inhibiting effect cells have on one another by using a similar kernel to (2.7). With w_ρ being the inhibition kernel, our assumption is that

$$w_\rho(\mathbf{x}) := \frac{\gamma}{C}e^{-\gamma\|\mathbf{x}\|}. \tag{2.13}$$

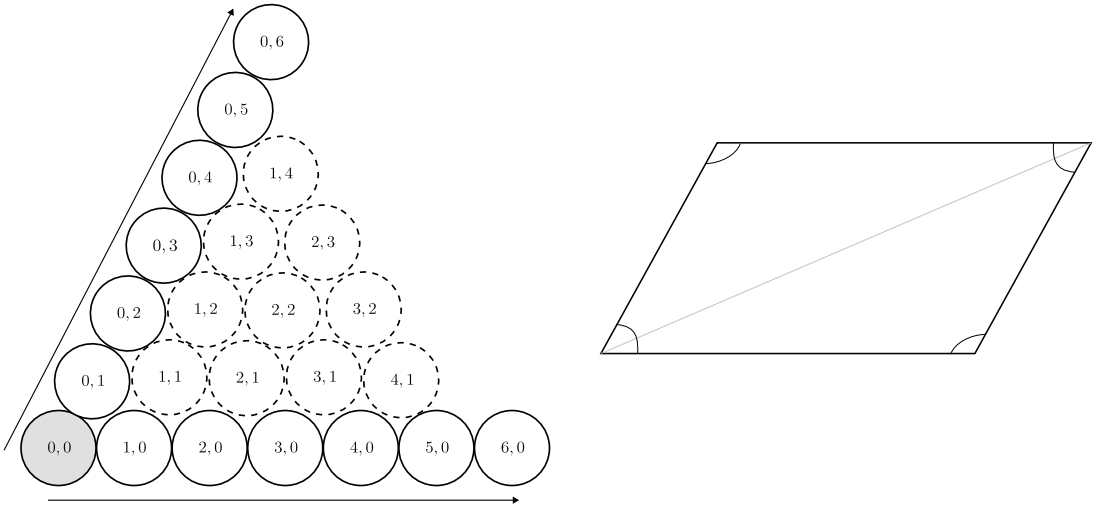

Fig. 2.1. Visualization of (2.18); we can fully index every steady state cell location in one sixth of the plane, and use the cosine law to calculate the distance from a cell located at site $(0,0)$ to a cell located at (n,m).

For simplicity, we choose in this study to lock the length scales of our two kernels to one another, i.e $\gamma = \varepsilon$. We thus get that the inhibiting effect the cells $j \neq i$ has on cell i is

$$\rho_i(t) = \varepsilon \sum_{j \neq i} e^{-\varepsilon \|\mathbf{x}_i(t) - \mathbf{x}_j(t)\|} \Longrightarrow \tag{2.14}$$

$$\rho_i(t) = \frac{1}{C}(g(\mathbf{x}_i(t)) - w(0)) \tag{2.15}$$

where $w(0)$ is subtracted since the cells do not self-inhibit. Furthermore we assume that the inhibition follows a simple logistical relationship, a common practice in this type of models (Browning et al., 2018; Fadai et al., 2020), motivated by the fact that the inhibition is directly proportional to the local cell density. We set the maximum inhibition to be one, implying that the local carrying capacity is one as well, i.e

$$0 \leq \rho_i(t) \leq 1, \tag{2.16}$$

$$J_i(t) = 1 - \rho_i(t). \tag{2.17}$$

where $\rho_i = 0$ is the case of a 2-dimensional universe devoid of neighbouring cells, and $\rho_i = 1$ represents the case of an infinite hexagonal lattice fully packed with identical circular cells resulting in maximum inhibition. Let $\mathrm{d}\eta(\mathbf{x})$ be the measure consisting of a δ-spike at every hexagonal lattice point. We can then determine ε by solving the equation

$$\int_{\mathbf{R}^2} w_\rho(\|\mathbf{x}_i(t) - \mathbf{x}'\|)\mathrm{d}\eta(\mathbf{x}') = 6\varepsilon \sum_{n=1}^{\infty}\sum_{m=0}^{\infty} e^{-\varepsilon\sqrt{n^2+m^2+nm}} = 1 \tag{2.18}$$

which is visualized in Fig. 2.1. Solving (2.18) numerically gives us $\varepsilon \approx 3.07$. With this ε, we provide an example of how the inhibition is calculated in Fig. 2.2. Keep in mind that solving (2.18) has imposed an assumption on the relationship between the decay rate and diffusion coefficient of the growth factor, a concession made in the name of convenience. Further note that if the problem was to be extended to three dimensions, a simple closed expression such as (2.18) would cease to exist.

Remember that the constant C encodes the relationship between the production and decay rates of GF, and thus plays a pivotal role in how neighbour stimulation affects population growth. Using (2.15), we express (2.12) as

$$G_i(t) = \lambda\Big(w(0) + C\rho_i(t)\Big) := \lambda_0 + \lambda_1\rho_i(t) \tag{2.19}$$

where the compound parameters λ_0 and λ_1 will be considered in our inference algorithm. Putting all components together, the cell division rate becomes

$$h_i(t) = J_i(t)G_i(t) = (1 - \rho_i(t))(\lambda_0 + \lambda_1\rho_i(t)). \tag{2.20}$$

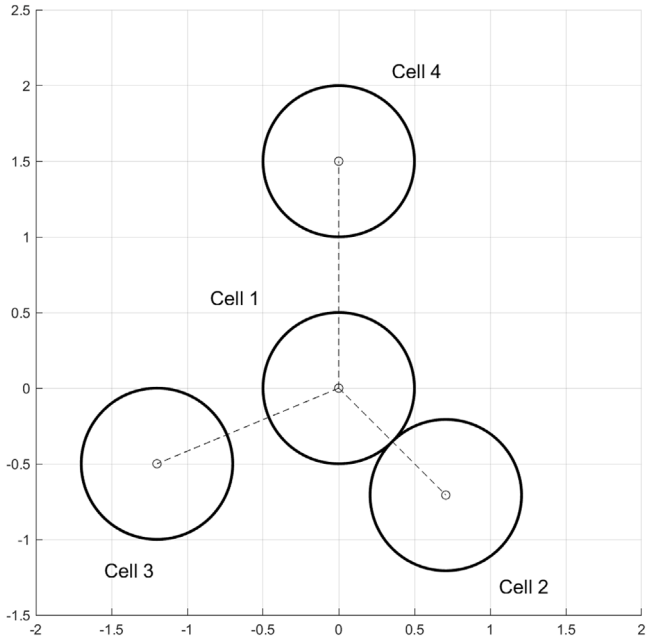

Fig. 2.2. An example of how contact inhibition on cell 1 is computed. $\mathbf{x}_1 = (0,0)$, and it has three neighbours, centred at
$\mathbf{x}_2 = (1,-1)/\sqrt{2}$,
$\mathbf{x}_3 = (-12,-5)/10$,
$\mathbf{x}_4 = (0,3)/2$.
The resulting contact inhibition becomes
$\rho_1 = \sum_{j=2}^{4} \varepsilon e^{-\varepsilon\|\mathbf{x}_i - \mathbf{x}_j\|} = 0.2302$.

Lastly, in order to observe a *strong* Allee effect where under a certain density the growth rate becomes negative, we must also introduce cell death. Consider the survival equation

$$\omega = \frac{D_i'(t)}{1 - D_i(t)}, \quad D_i(t_0) = 0, \tag{2.21}$$

where $D_i(t)$ is the probability that cell i has died at time t after its birth. Note that the solution to this equation is simply $D_i(t) = 1 - e^{-\omega(t-t_0)}$, i.e the cells lifespan is modelled by an exponentially distributed random variable. We let this random time be independent of the one governing cell division. Dropping subscripts and time-dependence, we get a

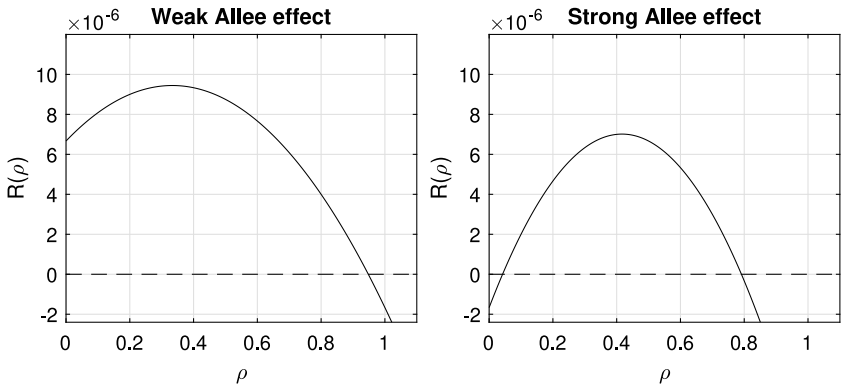

Fig. 2.3. The density-dependent per capita growth rate $R(\rho)$, given by (2.22). Parameters used are given by 4.1.

per-capita growth rate $R(\rho)$ of

$$R(\rho) = (1-\rho)(\lambda_0 + \lambda_1\rho) - \omega. \tag{2.22}$$

Alternatively, we can express (2.22) in terms of its roots;

$$R(\rho) = -\lambda_1\Big(\rho - \underbrace{\frac{\lambda_1 - \lambda_0 - \sqrt{4\lambda_1(\lambda_0-\omega)+(\lambda_1-\lambda_0)^2}}{2\lambda_1}}_{:=\alpha_1}\Big)\times$$
$$\Big(\rho - \underbrace{\frac{\lambda_1 - \lambda_0 + \sqrt{4\lambda_1(\lambda_0-\omega)+(\lambda_1-\lambda_0)^2}}{2\lambda_1}}_{:=\alpha_2}\Big)$$

where the roots $\alpha_{1,2}$ of this polynomial are the lower and upper Allee-thresholds, respectively. This also serves as a first-principles derivation of (1.3) in the introduction. We experience a strong Allee-effect when $\alpha_1 > 0$ - this corresponds to that for some ρ, we get $h(\rho) < \omega$. Examples of per capita-growth rate for weak and strong Allee effects can be seen in Fig. 2.3.

Note that $\lambda_1 > 0$ does not necessarily produce an Allee effect; in order for the per capita growth rate to have a distinct maximum for some $\rho > 0$, we need to have that $\lambda_1 > \lambda_0$. Thus, if a population sports a per capita growth rate where $0 < \lambda_1 < \lambda_0$, we say that this population does not exhibit an Allee effect.

3. Inference method

In this section we describe the method used for performing inference on the parameters λ_0, λ_1 and ω. We will implement a classical Metropolis–Hastings Bayesian method for estimating the model parameters. For a good introduction to these types of sampling methods, see Bishop and Nasrabadi (2006). Assume that we have observed a total of N cells in a series of K images. Throughout this section, remember that $\mathbf{x}_{ik}$ is the observed location of cell i at time t_k for $i = 1, \dots, N$ and $k = 1, \dots, K$.

It turns out we can find an exact posterior distribution for the cell death intensity ω if $t_{k+1} - t_k \equiv \Delta t$ is constant for all k. Let δ_i be the death time of cell i. From the exponentially distributed life lengths, we get from the Markov property that

$$P(\delta_i \in [t, t+\Delta t) \mid \delta_i \geq t) = P(\delta_i \in [0, \Delta t)) = 1 - e^{-\Delta t\omega}$$

meaning that the question "does cell i die in a time span of length Δt, given it was alive at time t?" can be probabilistically modelled using a Bernoulli random variable with parameter $\bar{\omega} = 1 - e^{-\Delta t\omega}$. Applying this to the entire population, then $\bar{\omega}$ is the parameter for a binomial random variable $D_k \sim \text{Bin}(N_k, \bar{\omega})$; i.e D_k models the number of deaths taking place during the interval $[t_k, t_k + \Delta t)$ given that N_k cells were alive at time t_k. Imposing a Beta prior distribution on $\bar{\omega}$ with parameters o_0, o_1, we get a conjugate posterior

$$\bar{\omega} \sim \text{Beta}(o_0 + \sum_{k=0}^{K-1} d_k, o_1 + \sum_{k=1}^{K-1}[N_k - d_k]), \tag{3.1}$$

$$\omega = -\frac{1}{\Delta t}\log(1-\bar{\omega}). \tag{3.2}$$

where d_k is the number of deaths observed in time interval k. If we wish for an explicit probability distribution for ω, we have it in

$$o_{0K} = o_0 + \sum_{k=1}^{K-1} d_k, \qquad o_{1K} = o_1 + \sum_{k=1}^{K-1}[N_k - d_k], \tag{3.3}$$

$$P(\omega_0 \leq \omega \leq \omega_1) = \frac{(o_{0K}+o_{1K}-1)!}{(o_{0K}-1)!(o_{1K}-1)!}\int_{\omega_0}^{\omega_1}(1-e^{-\Delta t r})^{o_{0K}-1}e^{-(o_{1K}-1)\Delta t r}\mathrm{d}r. \tag{3.4}$$

Now let β_{ik} be the number of cells born from cell i in the time interval $[t_k, t_{k+1})$. Keep in mind that one of the cells that i splits into inherits the index of its parent, thus making it possible for the cell labelled i to divide more than once on a time interval. Since the birth rate depends on the state of the system, β_{ik} follows a *non-homogeneous Poisson process*.

Let t_{i0} be either the birth time of cell i or the last time cell i divided, and β_i the time of its next birth. From (2.10), we know that for $t_{k+1} > t_k \geq t_0$ that

$$P(\beta_i \in [t_k, t_{k+1}) \mid \beta_i \geq t_k) = 1 - \exp\Big(-\int_{t_k}^{t_{k+1}} h_i(s)\mathrm{d}s\Big), \tag{3.5}$$

$$h_i(t) = (1-\rho_i(t))(\lambda_0 + \lambda_1\rho_i(t)). \tag{3.6}$$

Note that (3.6) cannot be directly evaluated between observations. To mitigate this, we fix the inhibition on cell i over the interval $[t_k, t_{k+1})$ to be what it was when observed at time t_k, i.e

$$\rho_i(t) \approx \rho_{ik} := \sum_{j\neq i} w_\rho(\|\mathbf{x}_{ik} - \mathbf{x}_{jk}\|), \qquad t \in [t_k, t_{k+1}). \tag{3.7}$$

Fixing ρ_{ik} in accordance with the observations let us calculate an approximate expression for the instantaneous birth rate (3.6) for cell i over the interval $[t_k, t_{k+1})$. Thus we approximate the accumulated birth rate as

$$H_{ik} = \int_{t_k}^{t_k+\Delta t}(1-\rho_{ik})(\lambda_0 + \lambda_1\rho_{ik})\mathrm{d}t = \Delta t(1-\rho_{ik})(\lambda_0 + \lambda_1\rho_{ik}). \tag{3.8}$$

We can now use (3.8) to approximate (3.5),

$$P(\beta_i \in [t_k, t_{k+1}) \mid \beta_i \geq t_k) \approx 1 - \exp\big(-H_{ik}\big). \tag{3.9}$$

Thus we get that the probability of cell i giving birth in $[t_k, t_{k+1})$ is approximately exponentially distributed with rate H_{ik}. For a more in-depth treatise on inference strategies on non-homogeneous Poisson processes, we refer to Li and Godsill (2021). With (3.8) in place, we can construct an approximate probability distribution from which we

can view β_{ik} as samples of. Calling this probability distribution B_{ik}, we have that

$$B_{ik} \sim \text{Poisson}(H_{ik}) \implies P(B_{ik} = b) = \frac{H_{ik}^b e^{-H_{ik}}}{b!}, \qquad b \in \mathbb{N}. \tag{3.10}$$

Given a sequence of observations ρ_{ik}, β_{ik}, this gives us the log-likelihood:

$$\ell(\lambda_0, \lambda_1 | \mathbf{x}, \beta) = \sum_{k=0}^{K-1} \sum_{i=1}^{N_k} \beta_{ik} \log(H_{ik}) - H_{ik} - \log(\beta_{ik}!). \tag{3.11}$$

The joint posterior distribution $q(\lambda_0, \lambda_1)$ for λ_0 and λ_1 does not have a closed form expression, and we will access the posterior distribution of these parameters by Markov Chain Monte Carlo. This algorithm is summarized in Algorithm 1. Throughout the algorithm, Z is a standard normally distributed random variable. Sampling from the posterior of all the parameters λ_0, λ_1 and ω is thus simple — use Algorithm 1 for a joint distribution over λ_0 and λ_1, and sampling ω from (3.1)–(3.2).

Also note that the posterior $q(\lambda_0, \lambda_1)$ is two-dimensional, and this opens up to the possibility of generating a surface plot over q by simply evaluating q for a large number of parameter configurations. We will make use of this as an alternate way to analyse our results.

Algorithm 1 Generate $\hat{S}$ samples q_s, $s = 1, \dots, \hat{S}$ from the distribution $q(\lambda_0, \lambda_1)$

Require: $\mu_0, \mu_1 \in \mathbf{R}$, $\sigma_0, \sigma_1 > 0$, $\sigma_s > 0$, $S \gg 0$, $S > \hat{S} > 0$
Ensure: $q_s \sim q(\lambda_0, \lambda_1)$
  $\log(\lambda_{01}) \leftarrow\sim \mathcal{N}(\mu_0, \sigma_0^2)$
  $\log(\lambda_{11}) \leftarrow\sim \mathcal{N}(\mu_1, \sigma_1^2)$
  for $s = 2 : S$ **do**
    $\log(\lambda_0^*) \leftarrow \log(\lambda_{0(s-1)}) + \sigma_{0s} Z$
    $\log(\lambda_1^*) \leftarrow \log(\lambda_{1(s-1)}) + \sigma_{1s} Z$
    $\alpha \leftarrow \min[1, \exp(\ell(\lambda_0^*, \lambda_1^*) - \ell(\lambda_{0(s-1)}, \lambda_{1(s-1)}))]$, ℓ as in (3.11)
    $\alpha^* \leftarrow \text{Unif}[0, 1]$
    if $\alpha > \alpha^*$ **then**
      $\lambda_{0s} \leftarrow \lambda_0^*, \quad \lambda_{1s} \leftarrow \lambda_1^*$.
    else
      $\lambda_{0s} \leftarrow \lambda_{0(s-1)}, \quad \lambda_{1s} \leftarrow \lambda_{1(s-1)}$.
    end if
  end for
  Keep the last $\hat{S}$ samples from $\lambda_{0(1:S)}$, $\lambda_{1(1:S)}$ respectively. Let these constitute $q_{1:\hat{S}}$.

4. In silico model

We chose to model our cell population using a system of SDE:s as presented in (2.1). Isotropic diffusion vastly simplifies some implementation aspects and given the homogeneity of the environment in the experimental data, it also serves as a fair assumption for an *in silico* model. At a particular moment in time t, the system evolves according to the following set of equations;

$$\mathrm{d}\mathbf{x}_i(t) = -\sum_{j \neq i} \nabla_{\mathbf{x}_i} u(\|\mathbf{x}_i(t) - \mathbf{x}_j(t)\|)\mathrm{d}t + \sigma \mathrm{d}W_i(t)., \tag{4.1}$$

$$u(r) = D_e \left[\left(\frac{\varphi(r)}{\varphi(r_0)} \right)^{2a} - 2 \left(\frac{\varphi(r)}{\varphi(r_0)} \right)^{a} \right]. \tag{4.2}$$

where $\varphi(r) : \mathbf{R}^+ \mapsto \mathbf{R}^+$ is a positive, monotonically decreasing function so that $\lim_{r \to \infty} \varphi(r) = 0$. We chose $\varphi(r) = e^{-r}$ - this choice of φ gives us the *Morse potential* as our model of interactions. r_0 is the equilibrium distance between two cells, and since we have already decided that $r_0 = 1$, the entire interaction potential is governed by two parameters; D_e (well depth) and a (well steepness).

4.1. Experimental setup

We simulate the system (4.1)–(4.2) using an Euler Maruyama scheme with a fine time-grid $\delta t = 1$, representing one *in silico* second, for a duration of 24 h. To mimic time-lapse microscopy data, we sample cell locations $K = 72$ times, representing 20 min between observations. We run this set up nine times for both modes of the Allee effect, with N_m cells spawned uniformly in circle of radius s_q in a 100×100 square "petri dish". The exact numbers are given by the bottom two rows of 4.1. In every time step, we propagate the particle system according to the Euler–Maruyama scheme;

$$\mathbf{x}_i(t + \delta t) = \mathbf{x}_i(t) + \delta t \left[-\nabla V(\mathbf{x}_i(t), t) \right] + \sqrt{\delta t} \sigma_i Z$$

Simultaneously, we simulate cell division and death for each cell. We remind ourselves of the Eqs. (2.9) and (2.21), and note that these are simple ODE:s that can be solved using an Euler forward scheme. So in every time step, we compute the evolution of birth and death probability as

$$B_i(t + \delta t) = B_i(t) + \delta t \left[h_i(t)(1 - B_i(t)) \right], \tag{4.3}$$

$$D_i(t + \delta t) = D_i(t) + \delta t \left[\omega(1 - D_i(t)) \right]. \tag{4.4}$$

A division or death is triggered for cell i whenever $B_i(t)$ or $D_i(t)$ passes a threshold b_i or d_i; here both b_i and d_i are standard uniformly distributed random variables. When a cell divides, a new b_i is generated and $B_i(t)$ returns to 0, see Fig. 4.1 for a demonstration. The daughter cell is placed half a cell radius away from the parent cell at a random angle, letting the interaction potential further push them apart.

Note that when cell division occurs, one of the new cells keep the index of the parent cell for the sake of efficiency. When a death is triggered, that individual is removed from the system. The simulations are run with the following parameters:

After every experiment is finished, we store three objects of particular interest. Let N be the total number of cells that were detected during the simulation. We first create the $N \times K$ matrix $\mathbf{R}$, where $\mathbf{R}_{ik} = \rho_{ik}$ as detailed in (3.7). The second object is the $N \times K$ matrix $\mathbf{B}$, where $\mathbf{B}_{ik} = \beta_{ik}$ (number of cells born from cell i in interval k). Lastly, we have a binary $N \times K$ matrix $\mathbf{L}$, where $\mathbf{L}_{ik} = 1$ if cell i was alive in observation k and 0 otherwise. With these three matrices, we have everything we need for Algorithm 1 and (3.1).

Table 4.1
Parameters used in our simulations.

Cell migration parameters:	$D_e = 0.00021$	$a = 3.5$	$\sigma_i = e^{-9/2}$
For weak Allee effect:	$\lambda_0 = \frac{1}{12} \cdot 10^{-4}$	$\lambda_1 = \frac{1}{4} \cdot 10^{-4}$	$\omega = \frac{1}{6} 10^{-5}$
For strong Allee effect:	$\lambda_0 = \frac{1}{12} \cdot 10^{-4}$	$\lambda_1 = \frac{1}{2} \cdot 10^{-4}$	$\omega = 10^{-5}$
Initial densities:	$s_n = 3 \cdot \sqrt{2^{9-n}}$	$n = 1, 2, 3$	
Initial cell counts:	$N_m = 2^{5+m}$	$m = 1, 2, 3$	

5. *In vitro* data

The *in vitro* data considered for testing our method is provided by Cell Tracking Challenge, where a large number of 2D video sequences of *in vitro* cell migration are available. The particular data set chosen for use here is "Fluo-N2DL-HeLa" of cervical cancer cells, first used in a study on phenotypic profiling using time-lapse microscopy (Neumann et al., 2010). Cervical cancer cells are round and of uniform size, thus giving us an ideal scenario for the inference algorithm as we assume all cells to be identical and circular. We will use two data sets, who served as hand annotated reference data for the challenge, giving us the closest to a ground truth possible for *in vitro* imaging. The two data sets are from the same cell line, consist of $K = 92$ images taken at 30 min intervals, and are of the same resolution. The only differing factor is initial cell density, see Table 5.1. Additionally, not a single cell died in either data set. As such, inference on the death rate ω for the *in vitro* experiments will be omitted.

Though the exact cell tracks are freely made available, we still need to normalize them so that an average cell radius equates to one in

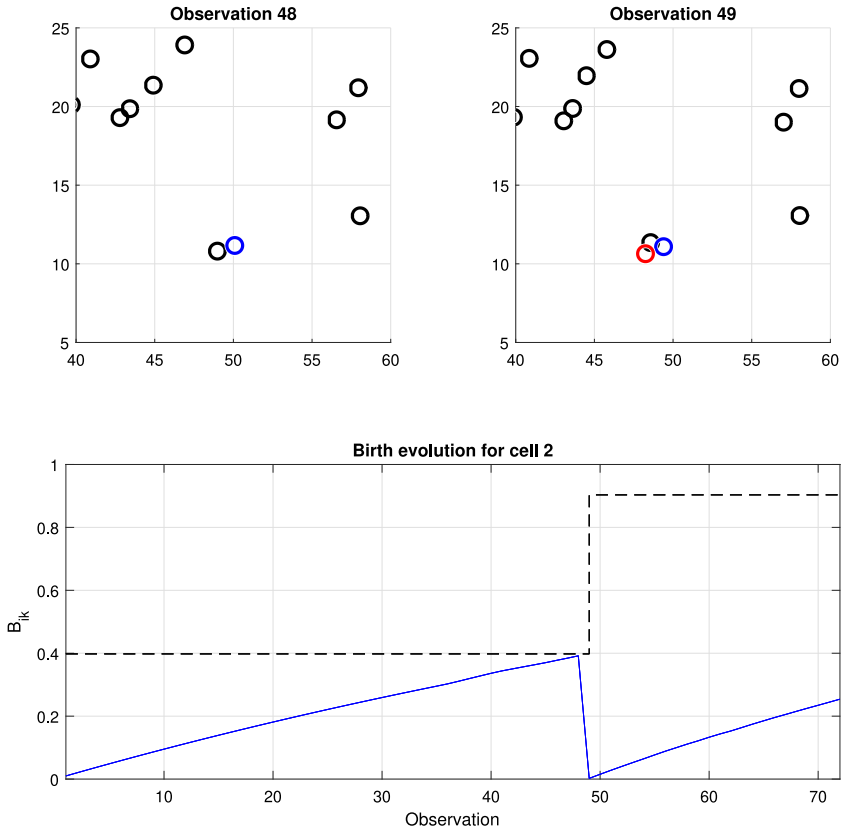

Fig. 4.1. A demonstration of how cell birth is modelled, for a simulation where cell 2 gave birth to cell 230 at observation $k = 49$. In every time step k, we forward simulate the birth rate $B_2(t)$ for cell 2 using (4.3). Once the birth rate hits the uniformly distributed birth threshold $b_2 \approx 0.4$, cell 230 was born and cell 2 was given a new birth threshold, $b_2 \approx 0.9$. Cell 2 is marked in blue, cell 230 in red, and all other cells are marked in black.

Table 5.1
Summary of the *in vitro* data sets.

Data set	Fluo-N2DL-HeLa/01	Fluo-N2DL-HeLa/02
N_1	43	137
N_{92}	125	363

order to directly apply our algorithm. We do this by computing the *radial distribution function* (RDF) for our image sequence. Enumerating the observation times as $k = 1, \dots, K$, the RDF for cell i at time t_k is computed numerically as

$$\mathrm{RDF}(r) = \frac{1}{2\pi r \mathrm{d}r} \sum_{k=1}^{K} \sum_{i=1}^{N_k} \sum_{j \neq i} \mathcal{I}\left[|\|\mathbf{x}_{ik} - \mathbf{x}_{ik}\| - r| < \mathrm{d}r/2 \right] \tag{5.1}$$

Here, $\mathcal{I}$ is the indicator function and $\mathrm{d}r = 0.5$ is a reasonably small radius 'shell', resulting in (5.1) returning the number density of cells within a distance $r \pm \mathrm{d}r/2$ of cell i at time t_k. RDF(r) for one of our data sets is visualized in Fig. 5.1.

6. Results

6.1. Results on in silico data

For each experiment, we run Algorithm 1 for 10,000 generations and discard the first 2,000 samples as burn-in. The remaining 8,000 samples constitutes our samples from the parameter posterior over λ_0 and λ_1. The posterior for ω is found using (3.1) with the uninformative prior $o_0 = o_1 = 0$. Let $\theta_{(n,m)} = \begin{bmatrix} \hat{\lambda}_0 & \hat{\lambda}_1 & \hat{\omega} \end{bmatrix}$ be the mode of the joint posterior for the data set with N_m and s_n initial condition. We propose to measure the goodness of fit of our results by a metric informed by the phenomenological nature of our model. Consider the L^2-norm between $\hat{R}(\rho)$, (2.22) parameterized by the inferred parameters, and $R(\rho)$ using the ground truth parametrization. Calling this metric $\Psi_{(n,m)}$ for experiment (n, m), we have that

$$\Psi^2_{(n,m)} = \int_0^1 \left(R(\rho) - \hat{R}_{(n,m)}(\rho) \right)^2 \mathrm{d}\rho \tag{6.1}$$

where $\hat{R}_{(n,m)}$ is (2.22) using the inferred parameters $\theta_{(n,m)}$. Note that the integrand in (6.1) is simply a fourth degree polynomial, and thus the integral is simple to evaluate. Results using this metric for the strong and weak Allee effect are found in Tables 6.1 and 6.2 respectively. Note that in these tables, we present the results for initiation circles with radius s_n as in Table 4.1 by their area πs_n^2.

We also wish to study if more insight can be gained by adding together all nine data sets featuring the strong and weak Allee effect respectively. In addition to inference on the two sets of nine data sets separately, we thus perform inference on these larger data sets as well. Figures using parameters inferred from this run can be seen in Fig. 6.1. We use the posterior modes, and they were found to be

$$\begin{aligned} &\text{Weak Alle effect:} \\ &\quad \lambda_0 = 9.05 \cdot 10^{-6}, \quad \lambda_1 = 2.20 \cdot 10^{-5}, \quad \omega = 1.66 \cdot 10^{-6}. \\ &\text{Strong Allee effect:} \\ &\quad \lambda_0 = 7.82 \cdot 10^{-6}, \quad \lambda_1 = 5.00 \cdot 10^{-5}, \quad \omega = 1.01 \cdot 10^{-5}. \end{aligned} \tag{6.2}$$

Additionally, we present the full posterior distribution over the death rate, seen in Fig. 6.2.

6.2. Results on in vitro data

The inference procedure used for the *in vitro* data described in Section 5 is identical to the set up used for our *in silico data*, barring

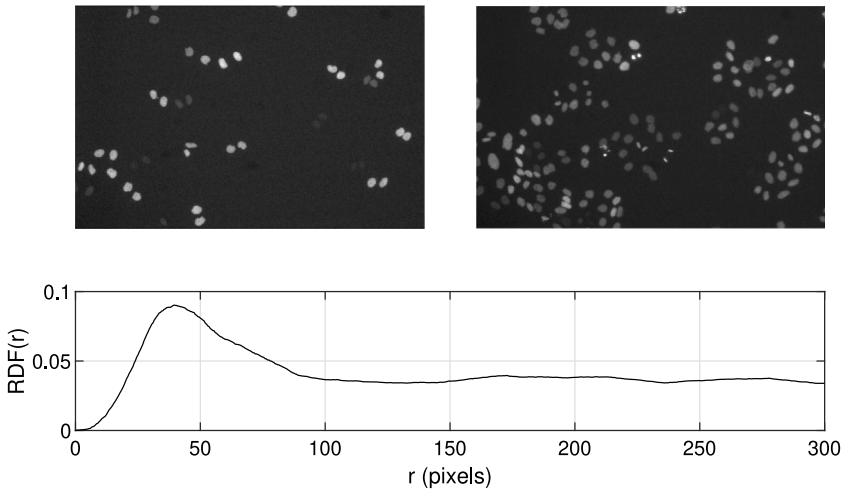

Fig. 5.1. The first and last frame of *in vitro* data set `Fluo-N2DL-HeLa/01`, along with the radial distribution function (5.1) for the data set in the bottom panel.

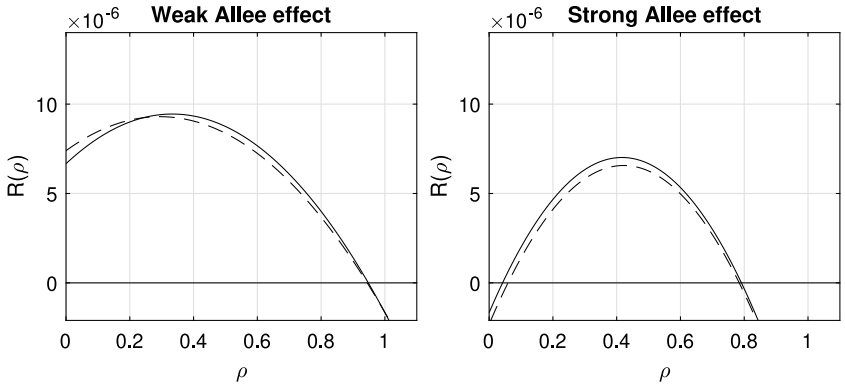

Fig. 6.1. Plots of (2.22) using the parameters found in (6.2). Ground truth in solid line (parameters given by 4.1), inferred curve in dashed line. The L^2 distance between these curves serves as our metric of fitness Ψ.

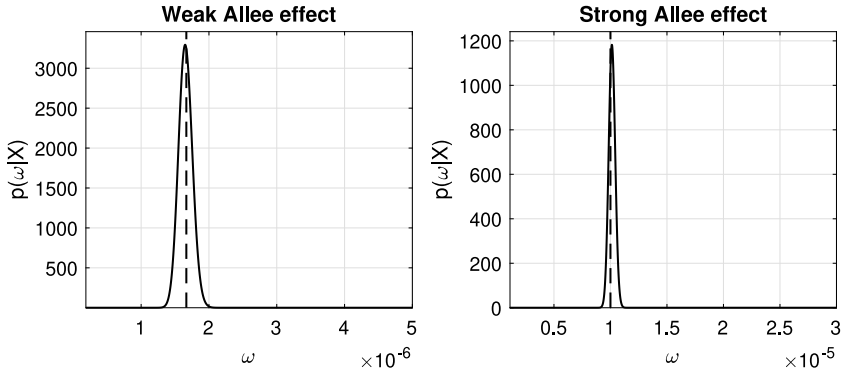

Fig. 6.2. Plots of the parameter posterior (3.4) pdf obtained from combining all nine data sets for the weak and strong Allee effect respectively. Ground truth marked with a dashed black line.

the fact that no cell death was detected in the considered data sets. As such, no strong Allee effect can be detected, as the presence of an extinction threshold require information on the population's death rate. Nonetheless, we attempt to fit the parameters λ_0 and λ_1 to our data, using 10,000 MCMC iterations, discarding a 2,000 iteration long burn-in. We consider the two data sets separately along with them added together. The resulting $R(\rho)$ for these three experiments are presented in Fig. 6.4. A summary of the parameter posteriors are found in Fig. 6.5, and visualization of the full joint posterior $q(\lambda_0, \lambda_1)$ in the case of `HeLa-02` is given by Fig. 6.6.

7. Discussion

7.1. Model development

The model used for the growth factor dynamics in this paper is the simplest type of reaction–diffusion equation one can formulate that accounts for the relevant processes governing the GF, and has been used in several earlier works (Gerlee et al., 2022; Menon and Korolev, 2015). The assumption of a linear relationship between the GF concentration and the stimulation of mitosis intensity (see Eq. (2.12)) also has precedent (Gerlee et al., 2022), although this relationship can undergo

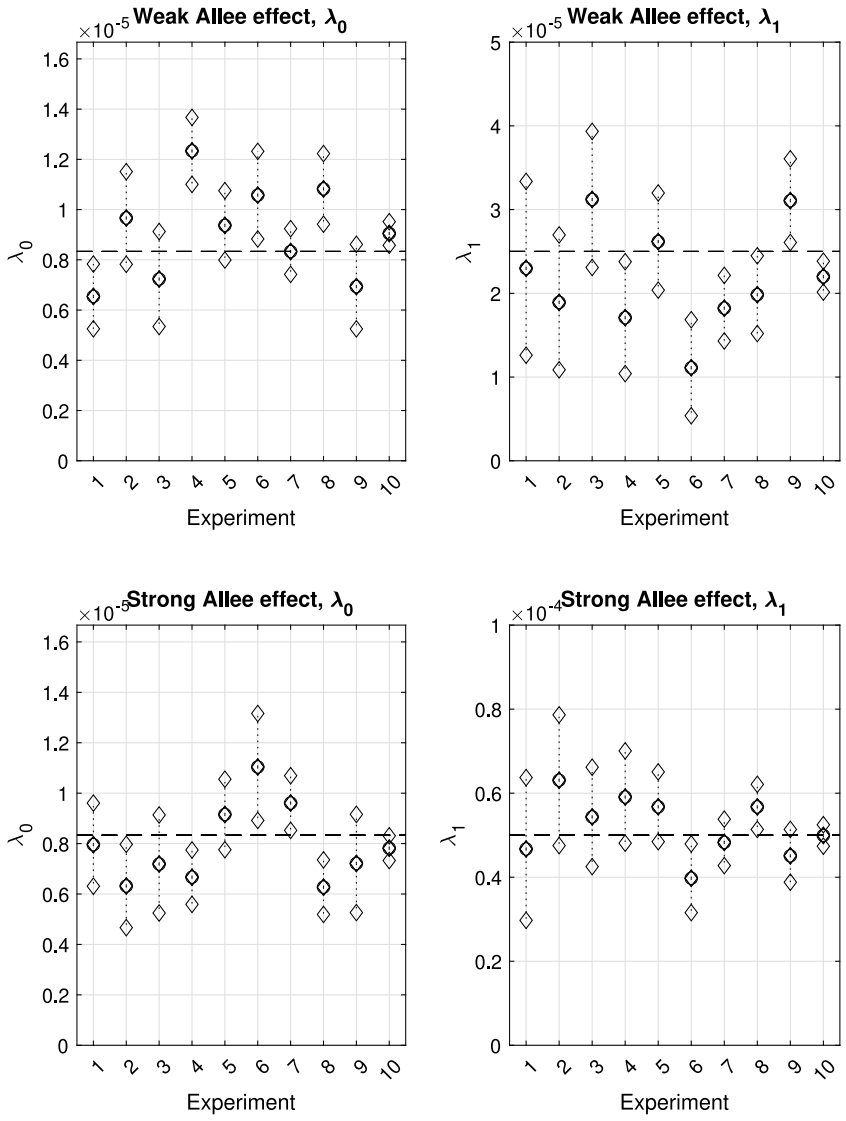

Fig. 6.3. Summary of results from Algorithm 1 applied to our *in silico* data. In every panel, experiment $1, \ldots, 9$ refer to our different initial conditions, counted row-wise according to Tables 6.1 and 6.2. Experiment 10 is the case for when all data sets were added together. The mode of the marginal posteriors for λ_0, λ_1 are marked with a circle; one standard deviation away is marked with a diamond. The ground truth is marked with a dashed black line.

Table 6.1
Weak Allee effect results for simulated data. In table cell (m, n), we have (6.1) for experiment (m, n). The bottom right cell is Ψ for when all data sets were added together.

$N_m \backslash \pi s_n^2$	2304π	1152π	576π	
64	$1.38 \cdot 10^{-6}$	$6.04 \cdot 10^{-7}$	$9.69 \cdot 10^{-7}$	
128	$1.38 \cdot 10^{-6}$	$6.15 \cdot 10^{-7}$	$1.59 \cdot 10^{-6}$	
256	$1.07 \cdot 10^{-6}$	$9.28 \cdot 10^{-7}$	$6.15 \cdot 10^{-7}$	
$\sum_{m,n}$				$3.33 \cdot 10^{-7}$

Table 6.2
Strong Allee effect results for simulated data. In table cell (m, n), we have (6.1) for experiment (m, n). The bottom right cell is Ψ for when all data sets were added together.

$N_m \backslash \pi s_n^2$	2304π	1152π	576π	
64	$1.94 \cdot 10^{-6}$	$1.70 \cdot 10^{-6}$	$1.43 \cdot 10^{-6}$	
128	$1.50 \cdot 10^{-6}$	$1.23 \cdot 10^{-6}$	$1.33 \cdot 10^{-6}$	
256	$4.24 \cdot 10^{-7}$	$8.07 \cdot 10^{-7}$	$1.45 \cdot 10^{-6}$	
$\sum_{m,n}$				$4.29 \cdot 10^{-7}$

some further scrutiny. GF molecules bind to cell surface receptors that transduce the signal to intra-cellular pathways that upregulate mitosis. This implies that above some threshold GF concentration all receptors are bound and additional GF does not increases the rate of mitosis further. A natural extension to the model would therefore be to assume that the relationship between GF concentration and the rate of mitosis is non-linear and saturating.

Under the assumption that the interaction time is short and the GF to cell ratio is high, a linear relationship suffices. However, one could choose to model the effect GF concentration has on mitosis intensity by letting $G_i(t)$ in (2.12) be a sigmoid, resulting in a saturation effect. An example of a model taking this into account is given by (1.5), which has precedence of usage in cancer research (Johnson et al., 2019). Additionally, letting $G_i(t)$ be sigmoid can model a threshold situation, where a certain amount of GF is required to accumulate before it impacts cell division rate.

The choice of using the same interaction kernel for GF uptake and contact inhibition factor was made for mathematical convenience. An interesting next step in developing the model is to instead let the kernels $w(\mathbf{x})$ and $w_\rho(\mathbf{x})$ function on different length scales. If we have

Table 6.3
Lower Allee thresholds estimated in the case of strong Allee effect for our *in silico* data sets. Experiment $1, \dots, 9$ refer to our different initial conditions, counted row-wise according to Table 6.1 and Table 6.2. Experiment 10 is the case for when all data sets were added together.

Truth	1	2	3	4	5	6	7	8	9	10
0.042	0.094	0.125	0.036	0.056	0.028	−0.021	0.015	0.078	0.081	0.0591

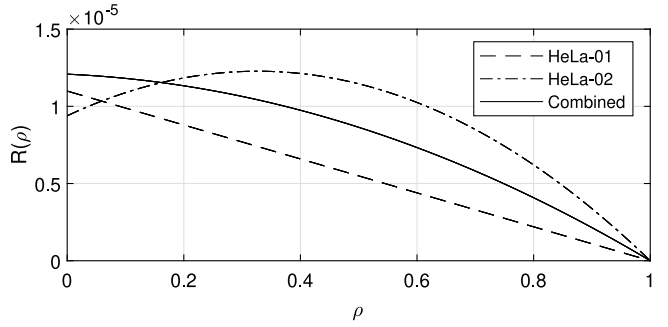

Fig. 6.4. $R(\rho) = (\lambda_0 + \lambda_1\rho)(1-\rho)$ fitted to the *in vitro* data. HeLa−01 in the dashed line, HeLa−02 in the dashed-dotted line, and both sets combined in the solid line.

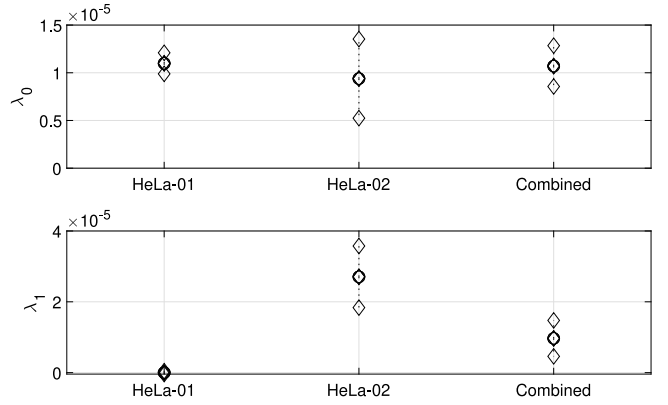

Fig. 6.5. The modes along with one standard deviation for each of our *in vitro* data sets. Note that λ_1 is very close to zero for HeLa−01, see Fig. 6.4.

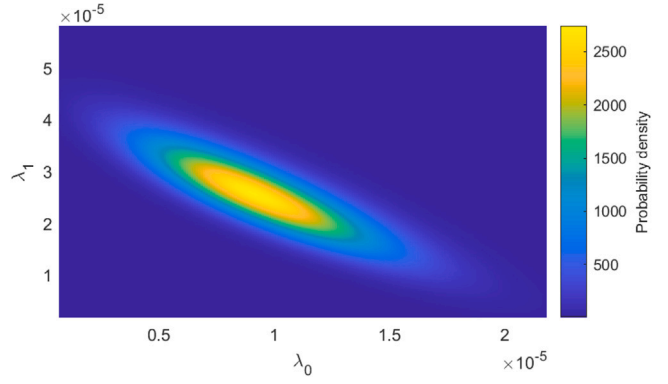

Fig. 6.6. Numerically computed posterior distribution $q(\lambda_0, \lambda_1)$ for the data set HeLa−02. Note a strong negative correlation between λ_0 and λ_1, resulting in the wide marginal likelihoods indicated in Fig. 6.5.

that

$$\rho_i(t) = \gamma \sum_{j \neq i} e^{-\gamma \|\mathbf{x}_i(t) - \mathbf{x}_j(t)\|}$$

we can still perform the same calculations as in (2.8) giving us $\gamma = 3.07$ without disturbing $\varepsilon = \sqrt{d_g/D_g}$. This leads to a much more involved per-capita reproduction rate of the form

$$h_i(t) = \left(\lambda_0 + \lambda_1 \sum_{j \neq i} e^{-\varepsilon \|\mathbf{x}_i(t) - \mathbf{x}_j(t)\|}\right)\left(1 - \gamma \sum_{j \neq i} e^{-\gamma \|\mathbf{x}_i(t) - \mathbf{x}_j(t)\|}\right)$$

introducing ε as a fourth parameter. It is still possible to construct an MCMC algorithm sampling from the posterior $q(\lambda_0, \lambda_1, \varepsilon)$, but the computational aspects become more complicated. First, the likelihood function for this model, analogous to (3.11) in this study, becomes geometrically more involved, perhaps facilitating the need for a more sophisticated sampling scheme than Algorithm 1. Secondly, we run a risk of further problems with parameter identifiability. Nevertheless, we aim for this model extension in future work.

Finally, the model we have studied does not take the different stages of the cell cycle into account. In Kynaston et al. (2022), the authors model the cell cycle for individual cells starting in a hypoexponential distribution, where a sequence of exponentially distributed holding times have to trigger before mitosis takes place. Comparing our model to this work, we make the progress through G1 depend on GF concentration, while S/G2/M takes place instantaneously. An interesting development could thus be to append a second holding time after β_i, modelling the time from growth finalization to cell division.

7.2. Inference algorithm

As previously alluded to, the algorithm we have implemented is of a basic Metropolis–Hastings type, giving us the benefit of straightforward implementation and little need for tuning hyper-parameters. We found that for the *in silico* experiments, it performed more than satisfactory given the relative simplicity of the task it was designed to solve.

There were a few pitfalls that can be addressed, however. When calculating the likelihood (3.11), every observation is given equal weight, despite some being arguably more valuable than others. For example, in denser data sets, $\rho_{ik} \approx 0$ is rarely featured. This could be an explanatory factor behind why the denser data sets generally performed worse when trying to approximate λ_0, as this is the chief parameter at play at low cell densities. Problems of this flavour is an active field of research in data science (Sapsis, 2020; Huan and Marzouk, 2014; Agrawal et al., 2019), where perhaps a method akin output-weighing as in Sapsis (2020) can be considered for future modifications of our sampling scheme.

A second issue is the problem of accurately determining the *extinction threshold* in the case of a strong Allee effect. Crucially, extinction thresholds are a notoriously difficult thing to quantify in any biological setting (Fieberg and Ellner, 2000). We speculate that such issues could perhaps be mitigated by giving extra weight to low-density observations, meaning that intelligent sample weighting can perhaps kill two birds with one stone here.

7.3. In silico results

Across the board, we find a very strong performance of our method on the *in silico* data. The best performance for both weak and strong Allee effect was found for experiments that struck a good balance between available data and cell density, with performance trailing of as density increases for estimating a weak Allee effect, and the inverse being true for strong Allee effect.

As previously discussed, the greatest uncertainty was in the cases of denser data sets, where λ_0 in general suffered much higher variance

in its estimate. Likewise, the very sparsest data sets returned greater uncertainty in λ_1, even though the mode of the posterior distribution was accurate in both the case of strong and weak Allee effect (see Fig. 6.3). The uncertain inference for low densities were particularly devastating for the strong Allee effect, resulting in some variance for the extinction threshold estimation (see Table 6.3). In one case, the inference method even proposed a weak Allee effect, likely due to the lack of low-density observations for this particular data set.

We see that the overall fit got slightly better when combining the data sets, as can be expected. The combined data sets include all combinations of high and low cell count coupled with high and low cell density, meaning that more levels of contact inhibition are presented to the inference algorithm.

7.4. *In vitro* results

Our results applying the algorithm to the *in vitro* data show some promise, and further highlight conclusions drawn from the *in silico* study. We note that `HeLa-01` had even lower cell count than our most sparse in silico experiments, numbered 1–3. For all of those experiments, we note a larger variance in the parameter posteriors when compared to our denser sets. Especially, estimating λ_1 in the case of a weak Allee effect proved especially troublesome, see Fig. 6.3. This might explain the great discrepancy detected between the inference on λ_1 in `HeLa-01` and `HeLa-02`.

In the case of `HeLa-02`, the variance in the marginal posteriors seen in Fig. 6.5 is much greater than for `HeLa-01`, indicating a potential *identifiability problem* for our model. This was the motivating factor behind the generation of Fig. 6.6, where we illustrate a noticeable covariance between λ_0 and λ_1 in the posterior distribution. Thus along the peak of the likelihood surface, there are many equally viable combinations of λ_0 and λ_1 that suits the data set. Still, the posterior indicate that an Allee effect is at play in this data set — unlike `HeLa-01`, $\lambda_1 \approx 0$ is given a next to zero likelihood.

The are several possible explanations to this. One could be that a certain concentration of growth factor has to be accumulated in order for it to have an up-regulating effect on the cell division rate. This could explain why no Allee effect is detected in `HeLa-01`, as that data set is too sparse to reach this level. The second explanation could be that the growth factor dispersion length scale ε is much further than what it was forced to be in order to satisfy (2.13). The model only takes GF produced by the immediate neighbours into account, but long-range dispersion remains a possibility. Both of these hypothesis can be tested by the model extensions discussed in Section 7.1. Finally, we acknowledge that the *in vitro* data set considered in this paper is quite small, and it is possible that Algorithm 1 could have honed in on a smaller portion of the parameter space given more information to work with.

The data set was chosen not only because of how cervical cancer cells satisfy our assumption of round cells well, but also because it had a gold standard truth available. Individual cell tracking is an exceedingly challenging problem (Ulman et al., 2017), especially so when determining familial relationship between the individual cells is important. This further highlights the need for high quality data processing methods when dealing with microscopy data. The *in silico* experiments confirmed that our method is capable of very precise inference using only modest amounts of data, as long as it is of high reliability.

It is crucial to note that no general statements on the presence of an Allee effect for cervical cancer can be made based in this limited study, be it *in vitro* or *in vivo*. The HeLa cells have evolved in a laboratory setting since the 1950's, making them a non-representative for cervical cancer on a whole (Masters, 2002). The main observation we make here is that for this particular set of data, a phenomenological Allee effect could be detected using a novel method. In order to draw strong conclusions on an Allee effect for a certain cell line, more data is necessary. Furthermore, conclusions on *in vivo* behaviour given *in vitro* studies of sample tissue require much finer considerations than the value of the parameters of our model can summarize.

8. Conclusion

In this article, we have derived a model for a spatial Allee effect for cancer cell populations. The derivation is based on the production of a common good by the cells, and an algebraic expression for the growth factor uptake is derived under simple assumptions. An MCMC sampling scheme was constructed to find the key parameters in the model based on imaging data, performing with high precision on moderately sized *in silico* experiments. For the limited trial on *in vitro* data, the results indicate the presence of an Allee effect, but parameter identification becomes a problem. Avenues of further research has been suggested, mainly on developing the model at the cost of added complexity. We also address the challenge of acquiring high enough volumes of dependable data, a possible bottleneck when conducting inference using single cell tracking in microscopy imaging.

Declaration of competing interest

The authors declare the following financial interests/personal relationships which may be considered as potential competing interests: Philip Gerlee reports financial support was provided by Swedish Foundation for Strategic Research.

Acknowledgements

This research is funded by SSF, Sweden grant SB16-0066. Special thanks to our master's student Anna Källsgård for help with Fig. 2.1.

References

Agrawal, R., Squires, C., Yang, K., Shanmugam, K., Uhler, C., 2019. Abcd-strategy: Budgeted experimental design for targeted causal structure discovery. In: The 22nd International Conference on Artificial Intelligence and Statistics. PMLR, pp. 3400–3409.

Basanta, D., Anderson, A.R., 2013. Exploiting ecological principles to better understand cancer progression and treatment. Interface Focus 3 (4), 20130020.

Bishop, C.M., Nasrabadi, N.M., 2006. Pattern Recognition and Machine Learning. Vol. 4. Springer.

Boukal, D.S., Berec, L., 2002. Single-species models of the Allee effect: Extinction boundaries, sex ratios and mate encounters. J. Theoret. Biol. 218 (3), 375–394.

Browning, A.P., McCue, S.W., Binny, R.N., Plank, M.J., Shah, E.T., Simpson, M.J., 2018. Inferring parameters for a lattice-free model of cell migration and proliferation using experimental data. J. Theoret. Biol. 437, 251–260.

Cassini, M.H., 2011. Consequences of local Allee effects in spatially structured populations. Oecologia 165 (3), 547–552.

Cleves, M., Gould, W., Gutierrez, R., Marchenko, Y., 2008. An Introduction to Survival Analysis Using Stata. Stata Press.

Courchamp, F., Berec, L., Gascoigne, J., 2008. Allee Effects in Ecology and Conservation. OUP, Oxford.

Da Silva, J.G., De Morais, R.M., Da Silva, I.C.R., Adimy, M., De Arruda Mancera, P.F., 2020. A mathematical model for treatment of papillary thyroid cancer using the Allee effect. J. Biol. Systems 28 (03), 701–718.

Delitala, M., Ferraro, M., 2020. Is the Allee effect relevant in cancer evolution and therapy? AIMS Mathematics 5 (6), 7649–7660.

dos Santos, R.V., Ribeiro, F.L., Martinez, A.S., 2015. Models for Allee effect based on physical principles. J. Theor. Biol. 385, 143–152.

Fadai, N.T., Johnston, S.T., Simpson, M.J., 2020. Unpacking the Allee effect: determining individual-level mechanisms that drive global population dynamics. Proc. R. Soc. Lond. Ser. A Math. Phys. Eng. Sci. 476 (2241), 20200350.

Fadai, N.T., Simpson, M.J., 2020. Population dynamics with threshold effects give rise to a diverse family of Allee effects. Bull. Math. Biol. 82 (6), 74.

Fieberg, J., Ellner, S.P., 2000. When is it meaningful to estimate an extinction probability? Ecology 81 (7), 2040–2047.

Gerlee, P., Altrock, P.M., Malik, A., Krona, C., Nelander, S., 2022. Autocrine signaling can explain the emergence of Allee effects in cancer cell populations. PLoS Comput. Biol. 18 (3), e1009844.

González-Olivares, E., Gonzalez-Yanez, B., Mena-Lorca, J., Ramos-Jiliberto, R., 2006. Modelling the Allee effect: are the different mathematical forms proposed equivalents. In: Proceedings of the International Symposium on Mathematical and Computational Biology BIOMAT, Vol. 2007. pp. 53–71.

Hörmander, L., 2009. The Analysis of Linear Partial Differential Operators IV: Fourier Integral Operators. Springer.

Huan, X., Marzouk, Y., 2014. Gradient-based stochastic optimization methods in Bayesian experimental design. Int. J. Uncertain. Quantif. 4 (6).

Johnson, K.E., Howard, G., Mo, W., Strasser, M.K., Lima, E.A., Huang, S., Brock, A., 2019. Cancer cell population growth kinetics at low densities deviate from the exponential growth model and suggest an Allee effect. PLoS Biol. 17 (8), e3000399.

Klebaner, F.C., 2012. Introduction to Stochastic Calculus with Applications. World Scientific Publishing Company.

Kynaston, J.C., Guiver, C., Yates, C.A., 2022. Equivalence framework for an age-structured multistage representation of the cell cycle. Phys. Rev. E 105 (6), 064411.

Li, C., Godsill, S., 2021. Sequential inference methods for non-homogeneous poisson processes with state-space prior. IEEE Trans. Signal Process. 69, 1154–1168.

Masters, J.R., 2002. Hela cells 50 years on: the good, the bad and the ugly. Nat. Rev. Cancer 2 (4), 315–319.

Menon, R., Korolev, K.S., 2015. Public good diffusion limits microbial mutualism. Phys. Rev. Lett. 114 (16), 168102.

Morris, D.W., 2002. Measuring the Allee effect: Positive density dependence in small mammals. Ecology 83 (1), 14–20.

Neumann, B., Walter, T., Hériché, J.-K., Bulkescher, J., Erfle, H., Conrad, C., Rogers, P., Poser, I., Held, M., Liebel, U., et al., 2010. Phenotypic profiling of the human genome by time-lapse microscopy reveals cell division genes. Nature 464 (7289), 721–727.

Obeyesekere, M.N., Zimmerman, S.O., Tecarro, E.S., Auchmuty, G., 1999. A model of cell cycle behavior dominated by kinetics of a pathway stimulated by growth factors. Bull. Math. Biol. 61 (5), 917–934.

Sapsis, T.P., 2020. Output-weighted optimal sampling for Bayesian regression and rare event statistics using few samples. Proc. R. Soc. Lond. Ser. A Math. Phys. Eng. Sci. 476 (2234), 20190834.

Simpson, M.J., Browning, A.P., Warne, D.J., Maclaren, O.J., Baker, R.E., 2022. Parameter identifiability and model selection for sigmoid population growth models. J. Theoret. Biol. 535, 110998.

Sun, G.-Q., 2016. Mathematical modeling of population dynamics with Allee effect. Nonlinear Dynam. 85, 1–12.

Tilman, D., May, R.M., Lehman, C.L., Nowak, M.A., 1994. Habitat destruction and the extinction debt. Nature 371 (6492), 65–66.

Ulman, V., Maška, M., Magnusson, K.E., Ronneberger, O., Haubold, C., Harder, N., Matula, P., Matula, P., Svoboda, D., Radojevic, M., et al., 2017. An objective comparison of cell-tracking algorithms. Nat. Methods 14 (12), 1141–1152.